Interface debonding characterization by image correlation integrated with Double Cantilever Beam kinematics

International Journal of Solids and Structures 55 (2015) 79–91

Contents lists available at ScienceDirect

International Journal of Solids and Structures

journal homepage: www.elsevier.com/locate/ijsolstr

Interface debonding characterization by image correlation integrated with Double Cantilever Beam kinematics

B. Blaysat [a,b], J.P.M. Hoefnagels [a,*], G. Lubineau [b], M. Alfano [b,c], M.G.D. Geers [a]

[a] Eindhoven University of Technology (TU/e), Department of Mechanical Engineering, PO Box 513, 5600MB Eindhoven, The Netherlands
[b] King Abdullah University of Science and Technology (KAUST), Physical Sciences and Engineering Division, Cohmas Laboratory, Thuwal 23955-6900, Saudi Arabia
[c] Department of Mechanical, Energy and Management Engineering (DIMEG), University of Calabria, Ponte P. Bucci, 44C, 87036 Rende, CS, Italy

ARTICLE INFO

Article history:
Available online 9 July 2014

Keywords:
Cohesive zone model
Interface mechanics
Identification
Double Cantilever Beam
Integrated Digital Image Correlation

ABSTRACT

A procedure is proposed for the identification of spatial interfacial traction profiles of peel loaded Double Cantilever Beam (DCB) samples, from which the corresponding traction–separation relation is extracted. The procedure draws upon recent developments in the area of non-contact optical techniques and makes use of so-called Integrated Digital Image Correlation (I-DIC) concepts. The distinctive feature of the I-DIC approach proposed herein is that the unknown degrees of freedom are not displacements or rotations, but the set of interfacial fracture properties describing the traction profile. A closed-form theoretical model is developed to reconstruct a mechanically admissible displacement field representing the deformation of the adhering layers during debonding in the DCB fracture test. The proposed modeling accounts for the spatial traction profile along the interface between the adherends using few degrees of freedom, i.e. crack tip position, maximum stress and size of the process zone. By minimizing the correlation residual with respect to the degrees of freedom, the full set of interfacial fracture properties is obtained through a one-step algorithm, revealing a substantial gain in terms of computational efficiency and robustness. It is shown that the identified traction profile can be effectively combined with the crack opening displacement to extract the corresponding traction–separation relation, i.e. the key input data for any cohesive zone model (CZM). The proposed procedure is validated by post-processing virtually deformed images generated through the finite element method. The robustness with respect to noisy data, as well as the low sensitivity to the initial guess, are demonstrated.

1. Introduction and motivation

Lightweight structures are made up of different materials (*e.g.* metal alloys, composites) and, as such, their mechanical behavior is strongly influenced by the presence of interfaces. The latter affect structural strength and stiffness, and to a large extent the fracture behavior. In fact, interfacial debonding of adjacent layers is one of the most important failure mechanisms in layered composite materials (Hutchinson and Suo, 1992; Evans and Hutchinson, 1995). Therefore, many research efforts have recently addressed the design and processing of high-quality interfaces securing structural integrity during service (Srikanth et al., 2006; Alfano et al., 2011, 2012; Almuhammadi et al., 2014), but also the implementation of predictive tools for the assessment of their reliability (Van den Bosch et al., 2006; Samimi et al., 2009).

Fracture Mechanics has been proven to be useful in understanding failure in layered materials (Hutchinson and Suo, 1992). However, the premise of a vanishingly small fracture process zone (FPZ) relative to the sample characteristic size is often not satisfied in practical applications, *i.e.* failure of bonded connections often occurs concurrent with the formation of a non-negligible FPZ in front of a macroscopic crack (Kolluri et al., 2011).

An alternative approach for the analysis of interfacial fracture and debonding, which accounts for the FPZ, is the use of a cohesive zone model (CZM) (Barenblatt, 1962; Dugdale, 1960). A cohesive zone is represented by a set of cohesive surfaces, which are held together by cohesive tractions. The tractions bonding the adherends across the interface may result from direct chemical (*e.g.* covalent bonds) and physical bonding (*e.g.* van der Waals forces), or may be caused by the presence of an interphase (*e.g.* adhesive layer[1]). The separation process is characterized by a

* Corresponding author.
E-mail address: j.p.m.hoefnagels@tue.nl (J.P.M. Hoefnagels).

[1] Note that the traction–separation relation might change with joint geometry (*e.g.* surface roughness or thickness of the substrates) and properties of the adhesive layer (*e.g.* thickness, bulk constitutive behavior).

http://dx.doi.org/10.1016/j.ijsolstr.2014.06.012
0020-7683/

traction–separation relation linking tractions to the relative displacements of the decohering surfaces.[2] With increasing separation, the traction will first increase and reach a maximum (cohesive strength), after which it decreases and eventually vanishes when the final opening displacement is reached. The CZM concept can be easily embedded in a finite element (FE) framework, and allows crack initiation to be simulated and growth in a wide range of materials and structures (Hillerborg et al., 1976; Needleman, 1987; Mohammed and Liechti, 2000; Van den Bosch et al., 2006).

Recent contributions, which reviewed advantages and limitations of the CZM approach, have highlighted that precise determination of the whole traction–separation relation is essential for the predictive nature of the model (Elices et al., 2002; Chandra et al., 2002; Park and Paulino, 2012; Wang, 2013). Initially, most papers focused on semi-empirical calibration procedures combining experimental testing performed on beam-like adhesive bonded specimens (*e.g.* Double Cantilever Beam, End Notch Flexure) and FE simulations of fracture, *e.g.* (Hutchinson and Evans, 2000). Specifically, the shape of the traction–separation relation has to be assumed *a priori*, from which the interfacial properties, such as cohesive strength and energy (*i.e.* the area enclosed by the traction–separation relation), were iteratively adjusted until a reasonable match between experiments and simulations was achieved. Typical experimental data used in such calibrations are the load–displacement curve, the specimen deflections and crack opening profiles (Mohammed and Liechti, 2000; Kafkalidis and Thouless, 2002; Tan et al., 2005). The resulting cohesive models provided satisfactory predictive capabilities. However, as reported in Chandra et al. (2002), Shen and Paulino (2011) and Park and Paulino (2012), empirical calibration procedures do not guarantee the uniqueness of the identified cohesive model. Direct methods have been proposed enabling the determination of the traction–separation relation without numerical post-processing. However, these methods typically require sophisticated experimental setups (Ivankovic et al., 2004; Bao and Suo, 1992; Sørensen, 2002; Sørensen and Jacobsen, 2003; Andersson and Stigh, 2004; Zhu et al., 2009; Gowrishankar et al., 2012). Some of these approaches (*cf* Sørensen, 2002; Sørensen and Jacobsen, 2003; Andersson and Stigh, 2004) recover the CZM features through the differentiation of *J*-integral, which is determined during the crack initiation regime in the experiment. Consequently, such approaches are heavily influenced by specimen pre-crack preparation artifacts.

Alternative approaches have been developed exploiting recent advances in the area of image processing, and the availability of low-cost CCD cameras, which enabled seemingly accurate measurements of surface displacement and rotation fields using Digital Image Correlation (DIC) (Schreier et al., 2009; Hild and Roux, 2006; Avril et al., 2008). A DIC algorithm typically correlates the local features of a pair of digital images searching for the displacement field which provides the best match between pixel intensities. This task is carried out by minimizing a norm of the residual between reference and deformed images. By using DIC, a large number of kinematic unknowns can be resolved compared to classical measurement devices (*e.g.* extensometers, encoders). The field information provided by DIC prompted the development of more versatile inverse parameter identification techniques combining FE simulations and full field displacement data. These techniques, also known as Finite Element Model Updating (FEMU), were initially proposed in order to identify elastic, elasto-plastic and visco-elastic constitutive properties of bulk materials (Avril et al., 2008). Subsequently, they were also used to supplement the existing methods for the identification of cohesive models, see Fedele et al. (2009), Valoroso and Fedele (2010), Gain et al. (2011) and Shen and Paulino (2011) to list a few. In these simulation-based identification frameworks, polynomial, exponential or bi-spline traction–separation relations were used. The unknown interfacial properties were then iteratively adjusted in order to minimize the difference between computed and measured surface displacements taken across the sample surface (Gain et al., 2011; Shen and Paulino, 2011) or a suitable sub-region (Fedele et al., 2009; Valoroso and Fedele, 2010).

In these existing approaches, essentially two minimization problems are solved, one associated with the DIC algorithm and the other to the FE-based equilibrium problem. As a result, uncertainties associated to both minimization loops sum up. This decoupling between the extraction of the displacement field and the identification of the interfacial properties may even lead to incorrect results. Indeed, interfacial properties may have a limited influence on the entire displacement field in some cases. Consequently, a small error in displacement measurements could result in significant errors in the identified traction–separation relation, as will be shown in this paper. Moreover, FEMU methods require a significant computing power since a complete non-linear FE simulation must be carried out at each iteration. In order to circumvent these issues, the DIC minimization procedure should be coupled directly to the final goal, *i.e.* the interfacial fracture properties.

Therefore, a DIC procedure is called for, which is based on the data retrieved from a simple test configuration, with minor experimental effort and expenditures, and reduced data post-processing. The aim of this work is to propose such a procedure, that complements existing methods and attempts to overcome some intrinsic limitations. The novel approach developed here exploits recent developments in the area of non-contact optical techniques and makes use of the so-called Integrated Digital Image Correlation (I-DIC) (Roux and Hild, 2006). The basic idea behind I-DIC is to introduce a regularization of the unknown displacement field through an efficient decomposition using a set of characteristic basis functions with unknown amplitudes (*i.e.* the degrees of freedom or *dofs*). However, the *dofs* are generally not kinematic variables as in *local* (Schreier et al., 2009) and *global* (Besnard et al., 2006) DIC, but rather mechanical quantities, *e.g.* stress intensity factors or elastic properties (Hild et al., 2009; Mathieu et al., 2012). Introducing this "mechanical" regularization, the gray level residual minimization directly yields the targeted mechanical interface properties (*i.e.* the unknown *dofs*), using a "one-step" algorithm. It is obvious that the success of I-DIC for identification of CZMs hinges on the proper incorporation of a mechanically admissible displacement field. In this paper, a closed-form theoretical framework is developed to reconstruct a mechanically admissible displacement field describing the kinematics of the adherends during a classical DCB fracture test[3] with only three *dofs*. The description accounts for the traction distribution across the interface, and the *dofs* represent the unknown interfacial properties. Once the *dofs* have been identified, the full displacement field within the sample can be reconstructed. As a result, by effectively combining the crack opening displacement and the identified traction profile, the corresponding traction–separation relation can be obtained. Since the proposed description displays a highly nonlinear dependency on the *dofs*, a suitable adaptation of the I-DIC framework is also proposed. To validate the I-DIC procedure and assess its computational efficiency and its robustness (with respect to noisy data and the choice of the initial guess), synthetic images of virtual DCB tests

[2] Note that the words *cohesive model* and *traction–separation relation* are invariably adopted throughout the paper to invoke the same concept.

[3] Since many standards exist nowadays for the DCB fracture test and since it is the mostly used, it has been chosen here as a first validation of an I-DIC dedicated to the CZM characterization. Updating the experimentation (and consequently updating the kinematics description) is of course possible, and opens new CZ characterization opportunity.

are post-processed with the I-DIC procedure. The paper is organized as follows. Section 2 introduces the proposed I-DIC identification procedure. Section 3 illustrates a closed-form theoretical description of the displacement field in the DCB fracture test. Section 4 describes the procedure adopted to generate synthetic experimental data (*i.e.* synthetic images) of the DCB tests. Section 5 presents the results, validation analysis and discussion, while concluding remarks and suggestions for future work are given in Section 6.

2. Identification of cohesive fracture properties using Integrated Digital Image Correlation (I-DIC)

2.1. Local and global approaches to Digital Image Correlation

A classical DIC algorithm correlates the local features of the reference (f) and the deformed (g) images, to identify the displacement field that provides the best match between pixel intensities in an area with a unique image pattern. The images (f) and (g) are matrices whose components represent gray level values for each pixel ($\underline{x}$). The pattern can be a randomly speckled surface obtained by spraying black and white paints on the object, or its natural surface texture (Hild and Roux, 2012). The unknown displacement field, $\underline{u} = \underline{u}(\underline{x})$, is identified by assuming that the surface speckle, or texture, of the object is not affected by the deformation, and passively follows the surface displacement of the underlying solid so that $f(\underline{x}) \approx g(\underline{x}+\underline{u})$, *i.e.* brightness is conserved during the deformation. Therefore, the objective within a conventional DIC algorithm is the determination of a displacement field that minimizes the correlation residual between (f) and (g).

However, stated in this form the problem is ill-posed, since $\underline{u}$ can only be determined in the direction of the intensity gradient.[4] Therefore, resolving the motion at the pixel level requires additional hypotheses on the *regularity* of the unknown displacement field. Moreover the brightness conservation equation is not strictly satisfied due to acquisition noise and fluctuations in light intensity (Mitiche and Bouthemy, 1996; Hild and Roux, 2006). For these reasons, an objective function $\mathcal{I}(\underline{u})$ is introduced to determine the optimal approximate displacement field $\underline{u}^{\text{opt}}$:

$$\underline{u}^{\text{opt}} = \underset{\underline{u}}{\text{Argmin}}\{\mathcal{I}(\underline{u})\} \quad \text{with} \quad \mathcal{I}(\underline{u}) = \int_{\Omega} \{f(\underline{x}) - g(\underline{x}+\underline{u})\}^2 \mathrm{d}\underline{x}, \qquad (1)$$

where the functional $\mathcal{I}(\underline{u})$ operates on $\underline{u}$. When the sum of the squared gray level residual is minimized, the unknown displacement field $\underline{u}^{\text{opt}}$ results.

In the earlier applications of DIC, the residual was evaluated over a domain Ω representing a small window of the considered region of interest, namely the zone of interest (ZOI). In this approach, often referred to as *local* DIC, the residual is minimized considering a subset-based reconstruction of $\underline{u}$ (*cf* Schreier et al., 2009). The unknown displacement field is retrieved after a collection of independent correlation computations for each subset, followed by interpolation of the displacements at the ZOI centers. No additional assumptions are enforced to restrict $\underline{u}$. In *local* DIC, the regularization is then implicitly embedded by the scale of the ZOI, *i.e.* the size of the subsets. However, *local* DIC suffers some drawbacks, *e.g.* the lack of displacement compatibility between adjacent subsets (which may lead to noisy reconstructed fields), and the sensitivity to the quality of the speckle pattern, which adversely affects the measured displacements (Shen and Paulino, 2011; Hild and Roux, 2012).

[4] Assuming small displacement, a first-order Taylor expansion leads to a linearized version of the optical flow equation, such that $f(\underline{x}) - g(\underline{x}) - \nabla g \cdot \underline{u}(\underline{x}) = 0$. As a result, the optical flow can only be determined in the direction of the intensity gradient. This is know as the *aperture problem* in DIC (*cf* Horn and Schunck, 1981; Hild and Roux, 2006).

In order to overcome these limitations, additional information can be included. For instance, a regularization can be introduced by assuming that the unknown displacement field is continuous. In this case $\underline{u}$ is decomposed over the whole region of interest (ROI) using a chosen set of basis functions which satisfy the continuity requirement, such that:

$$\forall \underline{x} \in \text{ROI}, \quad \underline{u}(\underline{x}) = \sum_{i=1}^{n} a_i \underline{\varphi}_i(\underline{x}), \qquad (2)$$

where $(a_i)_{1\leqslant i\leqslant n}$ are the *dofs*, while $(\underline{\varphi}_i)_{1\leqslant i\leqslant n}$ are the associated shape functions. The latter can be common Finite Element shape functions (*cf* Hild and Roux, 2006; Besnard et al., 2006). Evidently, several other choices are also possible depending on the specific problem at hand, such as X-FEM functions (*cf* Roux and Hild, 2006; Réthoré et al., 2008, 2009), polynomial basis functions (*cf* Neggers et al., 2014) or dedicated solutions, such as analytical expansions (*cf* Mathieu et al., 2012) or beam kinematic solutions (*cf* Hild et al., 2009; Leplay et al., 2010). The important point is that the gray level residual is minimized over a domain Ω representing the whole ROI and all the unknown *dofs* are obtained simultaneously in a single correlation step. This method is known as *global* Digital Image Correlation (G-DIC) (Hild and Roux, 2006; Avril et al., 2008).

2.2. Proposed identification approach based on I-DIC

Latest developments in the area of DIC gave rise a new approach, the so-called integrated (global) DIC (I-DIC). In this case the displacement field definition, and the DIC procedure, are tailored to a specific parameter estimation (Réthoré et al., 2009). The chosen *dofs* $(a_i)_{1\leqslant i\leqslant n}$ are directly related to the unknown material properties, and hence they are typically not displacements variables. As a result, the displacement field has to satisfy both constitutive and equilibrium equations. The I-DIC approach allows to identify, through a one-step algorithm, the unknown *dofs*, *i.e.* the unknown mechanical properties of interest. The main advantage is, as already discussed in Roux and Hild (2006), Réthoré et al. (2009, 2011) and Hild and Roux (2012), that the noise sensitivity is largely reduced. In recent work, I-DIC has been mainly introduced for the identification of stress intensity factors in cracked samples, by using shape functions based on numerical or analytical descriptions of the displacement field (Réthoré et al., 2009; Mathieu et al., 2012). To the best of our knowledge, there is no I-DIC approach aiming for the identification of interface debonding models.

This challenge, which requires a kinematic description of the interfacial traction profile, is developed in this paper. Specifically, we propose an iterative method for the identification of interface properties based on I-DIC. As for any I-DIC based identification procedure, two key elements are essential, *i.e.* (i) a mechanically admissible description of the displacement field (possibly characterized by a reduced number of *dofs*), and (ii) a suitable algorithm for the minimization of the image residual.

Although the complete description of the displacement field will be detailed in the next section, it is apparent from the discussion above that the displacements entail a highly nonlinear dependence on the interface *dofs*. This can be written as:

$$\underline{u} = \underline{u}(\underline{x}, (\Lambda_i)_{1\leqslant i\leqslant n}), \qquad (3)$$

where $(\Lambda_i)_{1\leqslant i\leqslant n}$ are the selected *dofs*, *i.e.* the unknown interfacial properties to be resolved. As a result, Eq. (2) is not directly applicable, and the minimization process requires a suitable adaptation.

This task is described in detail next. First, we assume that the cost function $\mathcal{I}(\underline{u})$, given in Eq. (1), remains valid for the nonlinear case. By introducing the nonlinear displacement field given by Eq. (3), one obtains

$$\underline{u}^{\text{opt}} = \underset{\underline{\Lambda}}{\text{Argmin}}\{I(\underline{\Lambda})\}, \quad \text{with} \quad I(\underline{\Lambda}) = \int_\Omega \{f(\underline{x}) - g(\underline{x}+\underline{u})\}^2 \mathrm{d}\underline{x}. \tag{4}$$

$I(\underline{\Lambda})$ is minimized by setting its derivative with respect to Λ_i equal to zero, $\forall i \in [1;n]$, which yields a system of nonlinear equations:

$$\forall i \in [1;n], \quad \int_\Omega \left\{ \frac{\partial}{\partial \Lambda_i}[g(\underline{x}+\underline{u})](f(\underline{x}) - g(\underline{x}+\underline{u})) \right\} \mathrm{d}\underline{x} = 0. \tag{5}$$

This problem is solved using a modified Newton–Raphson procedure. An iterative process is introduced, in which the *dofs* $\underline{\Lambda}$ are incrementally updated with the corrections $\underline{\delta\Lambda}$:

$$\begin{cases} \underline{\Lambda}^{\text{it}} \\ \underline{u}^{\text{it}} = \underline{u}(\underline{x}, \underline{\Lambda}^{\text{it}}) \end{cases} \quad \text{and} \quad \begin{cases} \underline{\Lambda}^{\text{it}+1} = \underline{\Lambda}^{\text{it}} + \underline{\delta\Lambda} \\ \underline{u}^{\text{it}+1} = \underline{u}(\underline{x}, \underline{\Lambda}^{\text{it}+1}). \end{cases} \tag{6}$$

Using a first-order Taylor expansion, the non-linear problem stated in Eq. (5) can be recast in a set of linear equations at iteration $(\text{it}+1)$:

$$\forall i \in [1;n], \quad \int_\Omega \left\{ \frac{\partial}{\partial \Lambda_i}[g(\underline{x}+\underline{u}^{\text{it}})](f(\underline{x}) - g(\underline{x}+\underline{u}^{\text{it}}) - \delta\Lambda_i \frac{\partial}{\partial \Lambda_i}[g(\underline{x}+\underline{u}^{\text{it}})]) \right\} \mathrm{d}\underline{x} = 0. \tag{7}$$

The derivatives of g with respect to the *dofs* can be expressed using the gradient of the image. This is done in a small-displacement context, which leads to $\underline{\nabla} \sim \underline{\nabla}_0$, and which justify the use of the reference image gradient $\underline{\nabla}_0 f$ to ensure a reasonable computational efficiency, following (Besnard et al., 2006; Roux et al., 2008):

$$\frac{\partial}{\partial \Lambda_i}[g(\underline{x}+\underline{u}^{\text{it}})] \sim \underline{\nabla}_0 f(\underline{x}) \cdot \frac{\partial \underline{u}^{\text{it}}}{\partial \Lambda_i}, \tag{8}$$

This yields the following linear system:

$$\underline{\underline{M}} \cdot \underline{\delta\Lambda} = \underline{b} \tag{9}$$

to be solved for $\underline{\delta\Lambda}$. Note that $\underline{\underline{M}}$ and $\underline{b}$ are defined in term of the extended "shape functions" $\underline{\varphi_i} = \frac{\partial \underline{u}^{\text{it}}}{\partial \Lambda_i}$ such that:

$$\begin{cases} M_{ij} = \int_\Omega \left\{ \underline{\varphi_i}(\underline{x}) \cdot \underline{\nabla}_0 f(\underline{x}) \cdot \underline{\nabla}_0 f(\underline{x}) \cdot \underline{\varphi_j}(\underline{x}) \right\} \mathrm{d}S \\ b_j = \int_\Omega \left\{ (f(\underline{x}) - g(\underline{x}+\underline{u})) \cdot \underline{\nabla}_0 f(\underline{x}) \cdot \underline{\varphi_j}(\underline{x}) \right\} \mathrm{d}S \end{cases} \tag{10}$$

The nonlinear procedure outlined above typically differs from a classical DIC approach through the evaluation of the shape functions. Indeed, in the present procedure the shape functions are not defined *a priori* but are redefined at each step of the iterative process. Another point of attention concerns the calculations. An analytical expression for this derivative is possible for some cases, but a numerical evaluation may offer more flexibility, especially for the present case, where the displacement reveals a highly non-linear dependence on the *dofs* $(\underline{\Lambda}^{\text{it}})$. The calculation of the shape functions is thus carried out as follows:

$$\underline{\varphi_i}(\underline{x}) = \frac{\underline{u}\left(\underline{x}, (1+\varepsilon)\Lambda_i^{\text{it}}, (\Lambda_j^{\text{it}})_{1\leqslant j\neq i\leqslant n}\right) - \underline{u}\left(\underline{x}, \Lambda_i^{\text{it}}, (\Lambda_j^{\text{it}})_{1\leqslant j\neq i\leqslant n}\right)}{\varepsilon \Lambda_i^{\text{it}}} \tag{11}$$

where ε denotes the magnitude of the (small) numerical perturbation. The next section presents the closed-form analytical kinematic description of the DCB test and the associated degrees of freedom.

The main steps involved in the proposed procedure are summarized in the flow chart given in Fig. 1. It essentially involves two algorithms, which are related to the I-DIC procedure, and to the kinematic description of the DCB test, respectively. The I-DIC procedure has been detailed in this section: based on a pair of images (f,g), the algorithm elaborates at each iteration (i) the right hand member $\underline{b}$ and (ii) the tangent operator $\underline{\underline{M}}$, which are based on the displacement $\underline{u}$ and the shape function $(\underline{\varphi_i})_{1\leqslant i\leqslant n}$ corresponding to the *dofs* $\underline{\Lambda}$. An iterative correction of the *dofs* $(\underline{\delta\Lambda})$ is then computed and the *dofs* are updated accordingly, $\underline{\Lambda} \equiv \underline{\Lambda} + \underline{\delta\Lambda}$. When this correction becomes small, the convergence criteria is satisfied and the problem is solved. The second algorithm, *i.e.* the kinematic description of the DCB test, is described in the next section.

3. A closed-form theoretical framework for the analysis of a DCB test

3.1. Description of a DCB test: from interface traction to 2D displacement field

The backbone of the proposed method is a suitable kinematic description of the DCB fracture test to be used in the I-DIC procedure (ASTM, 2007). A schematic depiction of a peel loaded DCB sample (mode I loading) with its interface at $y = y_0$ is given in Fig. 2(a). At the left end of the sample, a pre-crack of length a_0 has been introduced. The beams have thickness h^+ and h^-, respectively, width w and length $L = x_R - x_L$. The DCB is modeled as two beams whose kinematics is assumed to comply with the classical Bernoulli theory with corrections to account for nonlinear effects, originating from the large transverse deflections which may occur during crack growth (Kolluri et al., 2009). The sample beams are subjected to prescribed opening displacements $(v_p^+ \underline{e}_y, v_p^- \underline{e}_y)$ at the left end (*i.e.* at $x = x_L$), which corresponds to concentrated forces $F^+ \underline{e}_y$ and $F^- \underline{e}_y$ (see Fig. 2(a)). In addition, the interface condition entails an interfacial (normal) traction distribution $t(x)(t^+(x) = -t(x), t^-(x) = t(x))$ between the adherends at which an interfacial separation $\Delta(x)$ is corresponding, see Fig. 2(b)). Note that the knowledge of both the traction distribution $t(x)$ and the interfacial separation $\Delta(x)$ allows the recovering of the traction separation law (see Fig. 2(c)).

By stating the equilibrium equations, and imposing the boundary conditions (F^+, F^- and $t(x)$),[5] the neutral fiber displacement functions can be determined for both beams (details are given in Appendix A). Since there is no axial loading in the proposed Bernoulli beam model, all axial quantities are equal to zero and they are therefore not shown. The kinematic variables defining the motion of the beams at the neutral fiber are fully described by the beam transverse deflections, $v^+(x)$ and $v^-(x)$ and the cross-sectional rotations $\theta^+(x)$ and $\theta^-(x)$ (Fig. 2(d)). With the vertical displacement at both neutral fibers $v^+(x)$ and $v^-(x)$ known, the description of the 2D displacement field across the beams surface is easily obtained as:

$$\underline{u}(x,y) = \begin{bmatrix} u_x(x,y) = u^\square_{\text{rot}}(x,y) + u^\square_{\text{defl}}(x) \\ u_y(x,y) = v^\square(x) + v^\square_{\text{rot}}(x,y) \end{bmatrix}, \tag{12}$$

where "$\square$" refers either to the lower ("$-$", $y < y_0$) or upper beam ("$+$", $y > y_0$). The displacement due to cross-sectional rotations of both beams $(u^\square_{\text{rot}}, v^\square_{\text{rot}})$ have been taken into account through their strong forms

$$\begin{cases} u^\square_{\text{rot}}(x,y) = -(y - (y_0 \pm h^\square/2)) \sin\left(\theta^\square(x)\right), \\ v^\square_{\text{rot}}(x,y) = -(y - (y_0 \pm h^\square/2))\left(1 - \cos\left(\theta^\square(x)\right)\right) \end{cases} \tag{13}$$

with $\pm$ referring to $+$ for the upper beam and $-$ for the lower one. Finally, a correction upon the axial displacements $u^\square_{\text{defl}}$ due to large deflections is also included

$$u^\square_{\text{defl}}(x) = \int_{x_L}^{x} \left(\cos\left(\theta^\square(s)\right) - 1\right) \mathrm{d}s. \tag{14}$$

Notice that this procedure has a small computational cost compared to a full FE formulation, which would require the solution of an iterative problem, thereby considerably increasing the cost of

[5] In the current formulation, loads and displacements are prescribed at the beam neutral axis.

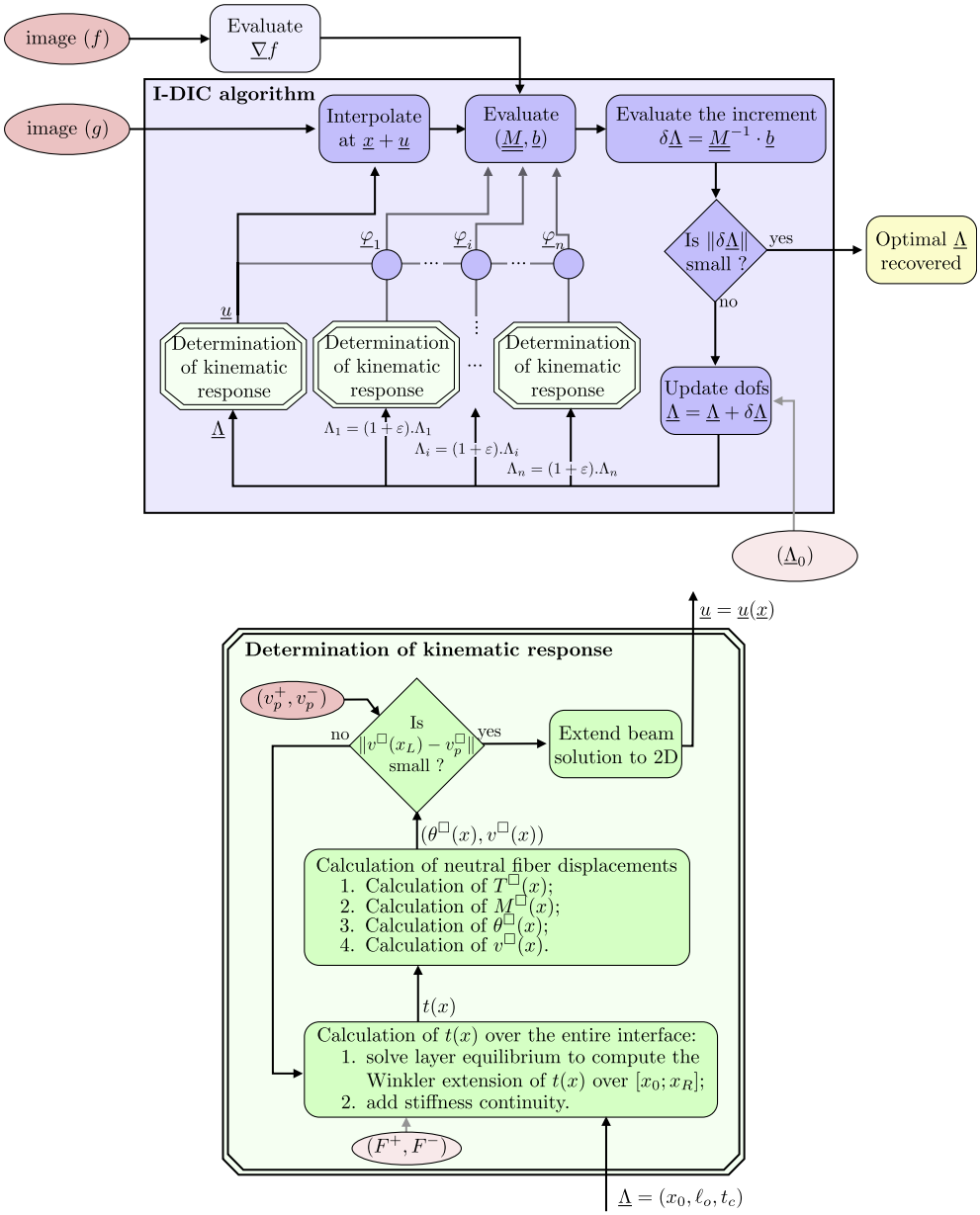

Fig. 1. Flow charts illustrating the proposed procedure adopted. Two nested iterative algorithms are involved: the top one iteratively solves the I-DIC problem, the bottom one concerns the calculation of the displacement field.

the quantification procedure. However, it should be noticed that alternative beam kinematics can be incorporated, for instance based on Timoshenko's theory (see Gowrishankar et al., 2012).

3.2. Parametrization of the interfacial traction profile

It is recognized that the adopted traction profile, $t(x)$, chosen to model the interface, greatly affects the robustness of the quantification procedure. We propose a partition into two distinct regions, the damaged (cohesive) region ($[x_L+a_0;x_0]$, called FPZ) and the undamaged one ($[x_0;x_R]$, called UDR), where the point x_0 denotes the physical crack tip position (Li et al., 2005).

In the first region, $x\leqslant x_0$, the tractions essentially represent the cohesive interactions accommodating the interfacial separation in the FPZ. In the second one, $x\geqslant x_0$, they represent the elastic response of the undamaged part of the interface. A schematic representation of the proposed partition is shown in Fig. 3.

Let us first introduce the traction profile chosen to represent the FPZ region. For this, a polynomial function has been selected:

$$t_{\mathrm{FPZ}}(x)=t_c\frac{(x-x_0)(x-(x_0-\ell_o))^2}{(x_c-x_0)(x_c-(x_0-\ell_o))^2}\Pi\left[\frac{1}{\ell_o}(x-(x_0-\ell_o/2))\right],$$
$$\text{with } x_c=x_0-\frac{\ell_o}{3}, \tag{15}$$

where ℓ_o is defined as the length of the process zone, t_c is the critical traction, x_c is the location along the x-axis where t_c is attained (*cf.* Fig. 3), and Π is the so-called rectangular function, which eclipses $t_{\mathrm{FPZ}}(x)$ outside the FPZ.

This polynomial description has been introduced because of its large versatility, *i.e.* by varying the *dofs* a large set of traction–separation relations can be recovered, as shown in Fig. 4, while yielding a compact definition of the traction profile with only 3 degrees of freedoms, *i.e.* x_0, ℓ_o and t_c. It is recognized that

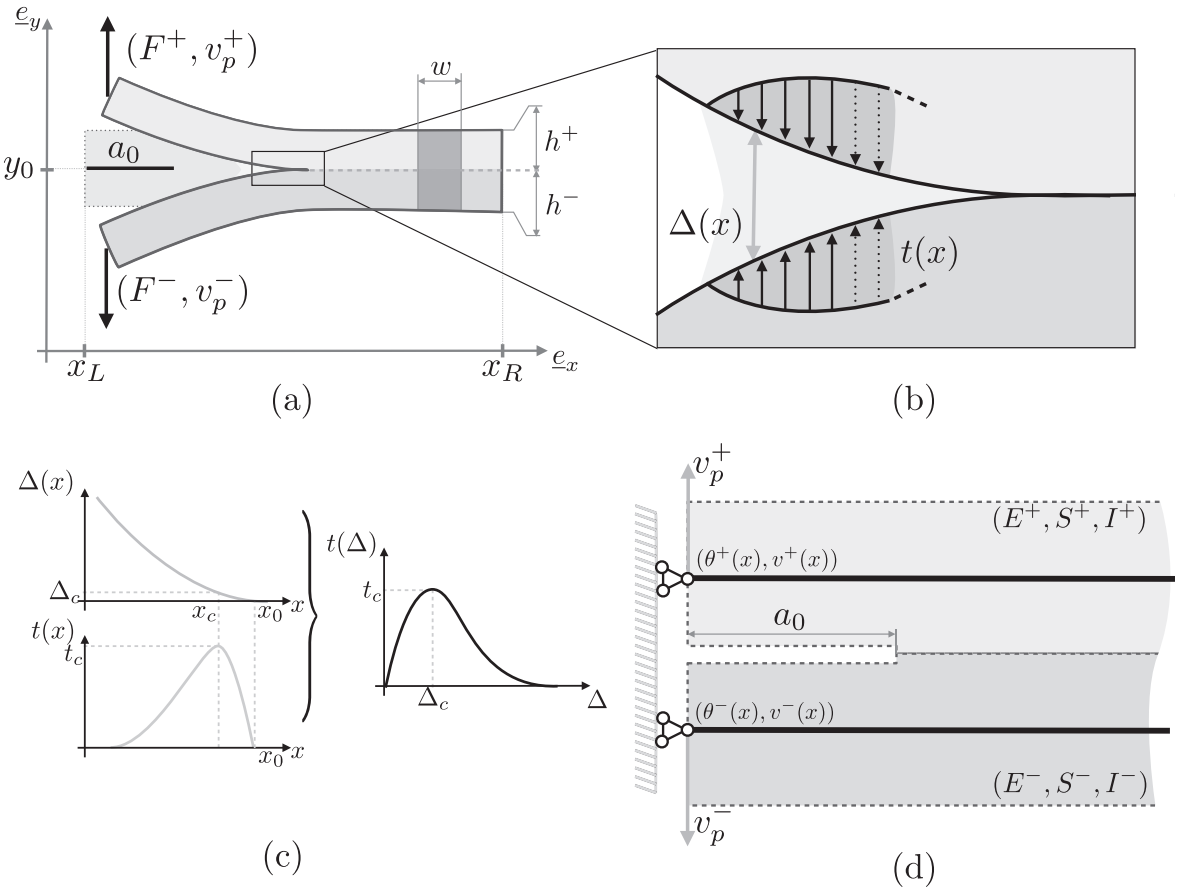

Fig. 2. Schematic representation of a DCB fracture test. (a) Geometry and boundary conditions. (b) Traction distribution at the interface ahead of the crack tip representing the interfacial cohesion during material separation. (c) Opening displacement and traction profiles along the fracture plane ($y = y_0$), and associated traction–separation relation. (d) Sketch of the beams with their neutral fiber, highlighting kinematic variables and notations used.

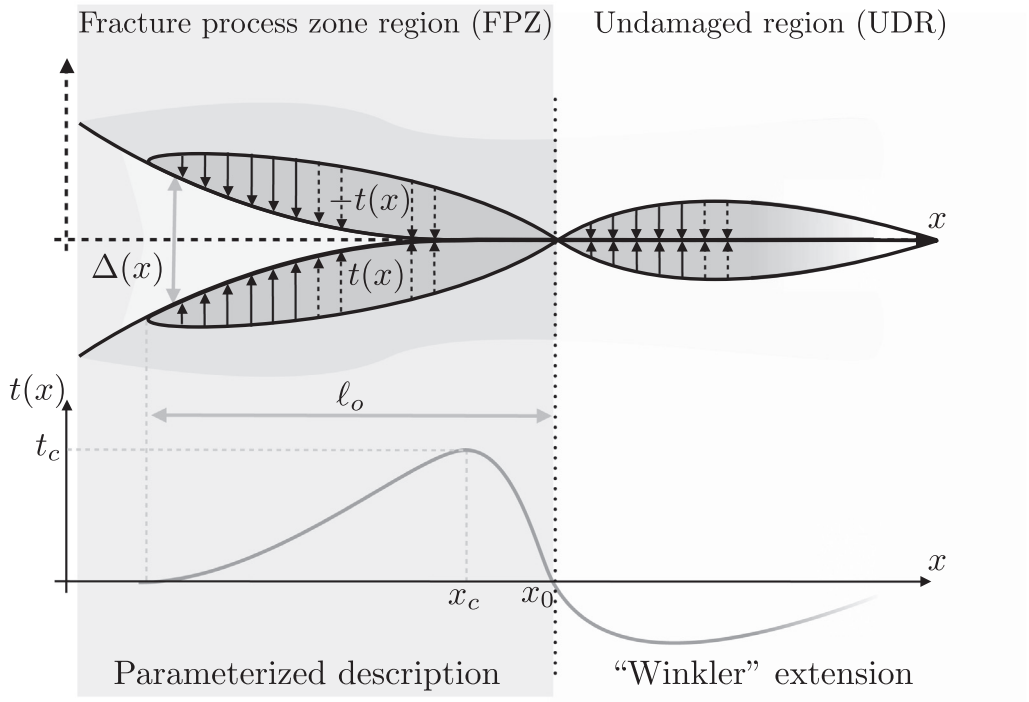

Fig. 3. Proposed partition of the traction profile along the sample interface. The damaged (cohesive) region, where material damage has occured, is described by a polynomial function with only 3 degrees of freedom, i.e. the length of the cohesive zone (ℓ_o), the peak stress (t_c) and the transition point (x_0) between the two regions. In the undamaged region (II), the tractions are described modeling the substrates as beams on an elastic foundation.

alternative choices for the parametrization are possible (see Swadener and Liechti, 1998; Mello and Liechti, 2004).

For the undamaged region (UDR), the interface stiffness is expressed as a beam on an elastic foundation, for which an analytical solution exists, *i.e.* the Winkler solution (*cf* Jumel et al., 2011), yielding the following (oscillatory) traction profile:

$$t_{\mathrm{UDR}}(x) = t_w^0 e^{-\lambda(x-x_0)} \sin(\lambda(x-x_0)), \tag{16}$$

where t_w^0 is linked to the magnitude of the traction and where λ can be interpreted as a damping coefficient.

So far, the traction profile is completely defined by five *dofs*, *i.e.* x_0, ℓ_o, t_c, t_w and λ. We can reduce the number of *dofs* further by enforcing additional equilibrium equations. Indeed, by simply adopting equilibrium to one arm of the sample, *e.g.* the upper layer ("$^+$"), we recover two additional equations. The first one is related to the force equilibrium in the y-direction:

$$\begin{aligned} &-F^+ - \int_{x_0-\ell_o}^{x_0} \{t_{\mathrm{FPZ}}(x)\}\mathrm{d}x - \int_{x_0}^{\infty} \{t_{\mathrm{UDR}}(x)\}\mathrm{d}x = 0 \\ &\Rightarrow -F^+ - \frac{9\ell_o t_c}{16} + \frac{\lambda t_w^0}{2} = 0, \end{aligned} \tag{17}$$

while the second one expresses the rotational equilibrium around x_0:

$$\begin{aligned} &F^+(x_0 - x_L) + \int_{x_0-\ell_o}^{x_0} \{(x_0-x)t_{\mathrm{FPZ}}(x)\}\mathrm{d}x + \int_{x_0}^{\infty} \{(x_0-x)t_{\mathrm{UDR}}(x)\}\mathrm{d}x = 0 \\ &\Rightarrow F^+(x_0 - x_L) + \frac{9\ell_o^2 t_c}{40} + \frac{\lambda^2 t_w^0}{2} = 0. \end{aligned} \tag{18}$$

It is apparent that, through Eqs. (17) and (18), the Winkler parameters (λ, t_w^0) can be expressed as a function of x_0, ℓ_o, t_c, which are the parameters of interest describing the interfacial traction profile.

In addition, interfacial stiffness continuity has been enforced between the two regions, as described in Appendix B, whereby the number of *dofs* has been preserved.

With the proposed partition of the interface behavior it is possible to describe the entire interfacial traction profile with only three *dofs* and subsequently compute the complete 2D displacement field over both sample layers. This kinematic description has been incorporated in the I-DIC procedure, see Fig. 1(b). The algorithm titled "Determination of kinematic response" yields, for a set of interfacial parameters (x_0, ℓ_o, t_c), the 2D kinematic response $\underline{u}(\underline{x})$, satisfying the prescribed displacement at the left end of the specimen as well as equilibrium. The problem is solved with a prescribed force at the left end of both arms of the specimen. The procedure is initialized by using the applied (F^+, F^-). Consequently, this necessitates the proposed iterative scheme, in order to ensure the satisfaction of the prescribed displacement boundary condition.

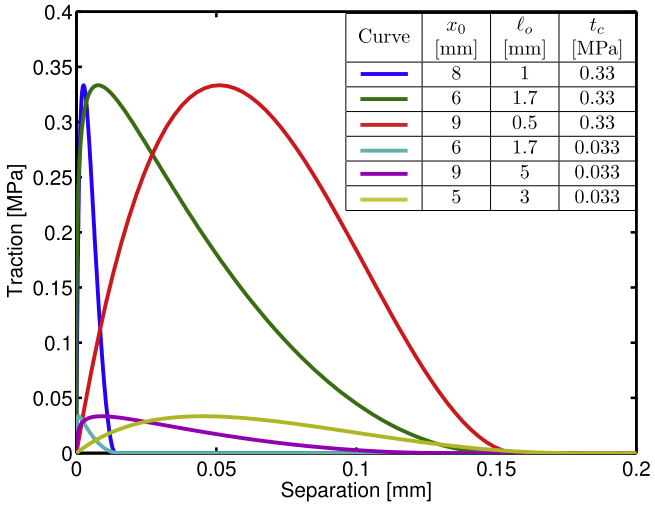

Fig. 4. Model traction–separation relations generated by varying the degrees of freedom employed to represent the traction profile within region I of the sample interface, *i.e.* ℓ_o x_0 and t_c.

4. Generating synthetic data for procedure validation

4.1. FE modeling and development of pseudo-experimental displacement data

Synthetic data will be used for validation purposes. To this aim, we focus on the DCB specimen that was studied in Kolluri et al. (2009). The analyzed sample consists of steel substrates ($E^+ = E^- = 210$ [GPa], $\nu^+ = \nu^- = 0.35$ [–]), bonded with a thin adhesive layer. The geometrical specifications are: $h^+ = h^- = 0.1$ [mm], $w^+ = w^- = 3$ [mm], $a_0 = 3$ [mm] and a length of 20 [mm] (*cf* Fig. 2). The synthetic images, to be post-processed with the proposed procedure, are generated from a FE model of this DCB sample. The strategy adopted to construct the synthetic images involves the following steps: (i) a FE simulation of the DCB fracture test for a given traction–separation relation; (ii) subsequently, extraction of the synthetic reference image (f) obtained by virtually attaching an artificial pattern to the specimen domain; and (iii), deformation of the reference pattern (f) using the FE displacement field, yielding the deformed synthetic image (g). These steps are detailed next.

A 2D finite element model has been used for the sample, with plane stress quad elements for the substrates[6] and a single row of cohesive elements for the adhesive layer. The latter utilizes the enriched formulation recently proposed in Samimi et al. (2009). Vertical displacements were prescribed at the left end of both sample arms (v_p^+, v_p^-) to induce the desired peel loading condition, and the problem was solved assuming a large displacement hypothesis. The efficiency of such a numerical approach has already been demonstrated in Kolluri et al. (2012).

Four cases are analyzed, which differ only through the adopted "physical" traction–separation relation. In the first case study (*i.e.* #1), the interface behavior is described using a bi-linear traction–separation relation; in the remaining ones (*i.e.* #2–4), a potential based cohesive model was employed (*cf* Park et al., 2009). Details on the selected set of cohesive parameters for each case are given in Fig. 5. In order to use suitable parameters for the problem at hand, we selected input traction–separation relations that are in the range of the physical response identified in Kolluri et al. (2012). Nevertheless, large differences between the 4 cases are incorporated, see Fig. 5. The FE global load–displacement responses obtained for each application are shown in the insert in Fig. 5. The figure also highlights the loading steps selected to extract the displacement data that is used to generate the deformed synthetic images (g). These have been chosen in the post-peak regime of the global response to ensure that the deformed images incorporate a fully developed FPZ. It is thereby assumed that the resulting images contain all the information needed to identify the complete traction profile.

4.2. Generating reference and deformed synthetic images

The reference image (f), illustrated in Fig. 6(a), is the superposition of an artificial pattern on top of the specimen domain. This

[6] Finite element discretization was carried out using 10 2D elements over each layer thickness and 1000 along the length direction of each layer.

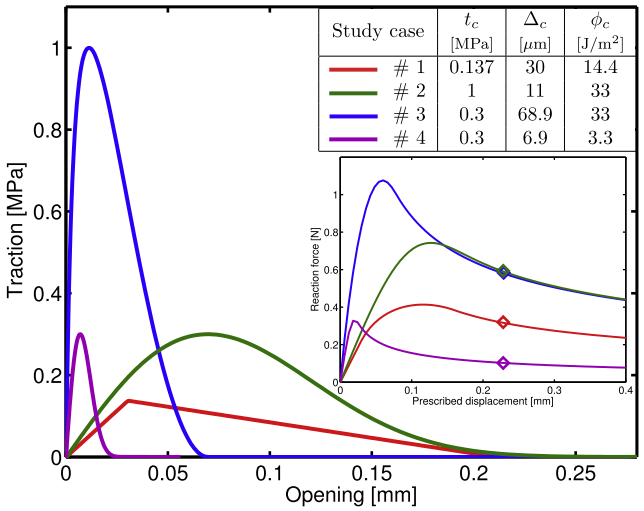

Fig. 5. Assumed "physical" tractions separation laws used for the validation analysis. The inserted table gives the values of the traction peak t_c, the associated critical opening Δ_c and the work of separation ϕ_c. The inserted figure shows the global force - displacement response obtained through the finite element simulations of the four case studies. The symbols denote the loading steps at which the displacement fields were extracted to generate the deformed synthetic images (g).

pattern is defined as the combination of three Gaussian fluctuation fields, which have identical mean and standard deviation respectively set to 16.67% and 10%. These three fluctuation fields are then interpolated to the pattern using different length scales, which are 2, 8 and 32 pixels (Dainty, 1977). The images resolution is set to 1024×100 pixels, with a minimum pixel size around 5 [μm]. The next step consists in "deforming" the reference pattern using the FE solution to get the (noiseless) deformed image (g). This step is detailed on the basis of case study #1. The FE maps of the 2D displacement field corresponding to the prescribed opening of the DCB are given in Fig. 6(b). These displacements are subsequently applied to the reference pattern, which thereby deforms according to the computed displacement field. In order to closely resemble actual experimental conditions, white noise is also added to the deformed image (Fig. 6(c)). As stated in Hild and Roux (2012), there is no noticeable difference between applying noise on both (f) and (g) or a double noise on (g) (or (f)) only. The added white noise is defined through a Gaussian distribution, with a mean equal to 0 and a standard deviation σ ranging up to 15%. It should be recognized that the introduced noise reflects poor measurement conditions, since the standard deviation of usual CCD or CMOS cameras is typically of the order of 1% of the dynamic range. This choice allows to assess the robustness of our approach.

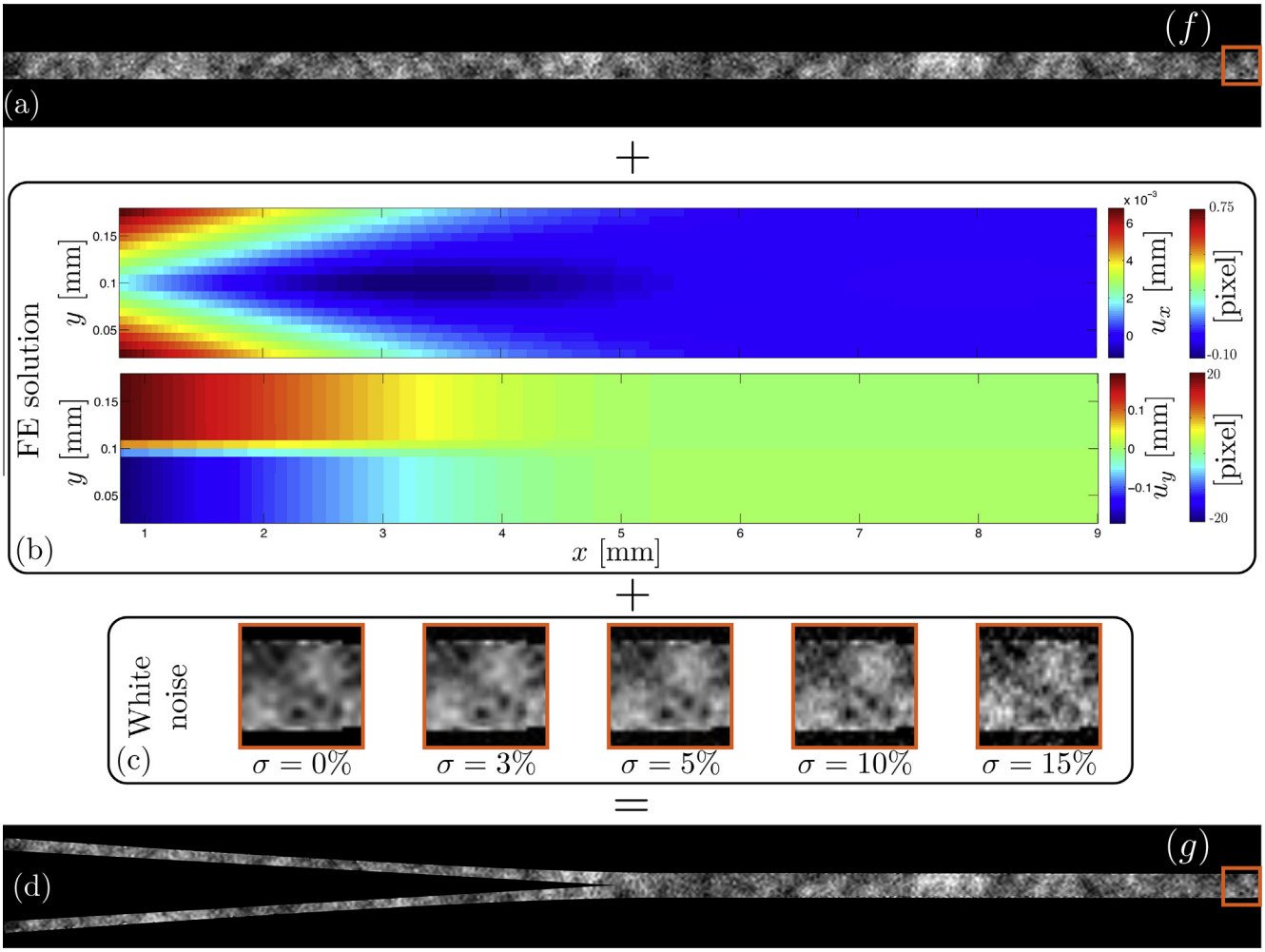

Fig. 6. Procedure to generate synthetic undeformed (f) and deformed (g) images. An artificial pattern is created and superposed on the sample mesh, which defines the reference image (f) (a), on which the displacement fields obtained through FEA (b) augmented with additional white noise (c) are applied in order to obtain the deformed image (g) (d). Images specifications are 1024×100 pixels, with 8-bit depth.

5. Results and discussion

The mechanically admissible kinematic description of the DCB test is now used in conjunction with the generated synthetic data in the I-DIC algorithm. First the results obtained from the proposed procedure, and the associated error maps, are presented. Next the sensitivity of the method with respect to the initial guess and noisy data is thoroughly investigated.

5.1. Results of the proposed procedure

An important outcome of the minimization procedure is that, apart from the optimized *dofs* values and the associated displacement field, a map of the residual, *i.e.* $f(\underline{x}) - g(\underline{x} + \underline{u}^{\text{opt}}(\underline{x}))$ can also be obtained. The residual map emphasizes (localized) systematic errors, which may result from an inappropriate kinematic description. Fig. 7 illustrates the final DIC residual for case study #1. A small homogeneous distributed mismatch can be observed, which corresponds in amplitude to the added white noise present in the image (g). The absence of any systematic pattern in the residual field indicates that the kinematics description used within the I-DIC is rich enough to describe the fracture process.

The quality of the kinematic description can be investigated more directly from the displacement error maps. Fig. 8 presents these maps for case study #1. The error components are noticeably low, below 2.10^{-4} [mm] in the y-direction (2.10^{-5} [mm] in the x-direction). With a pixel size of 8.8 [μm] the error is thus less than 2% of a pixel in the y-direction (0.2% of a pixel in the x-direction). Moreover, since the pixels are clearly visible in Figs. 7 and 8, it becomes apparent that a high image resolution is not required for the proposed procedure. Finally, the knowledge of the error of the displacement field highlights some important features of the procedure, which are not visible in the residual maps in Fig. 7. The map of the x-component of the displacement error illustrates that the non-linearity associated to the large deflection is well captured. The fact that the sign of the error switches from positive to negative on both error maps indicates that there is still a mismatch, but the associated order of magnitude remains small. In addition, localized errors close to the position of the applied interface conditions can be observed, especially in the x-component of the displacement error map Fig. 8(a), which indicates that the adopted kinematic description is not incorporating these local phenomena. As shown in Fig. 7, these details are masked through the white noise in the residual map. Consequently, adding a more detailed description, with more *dofs*, would probably result in a more noise-sensitive procedure.

The goal of the proposed procedure is, however, not to recover the displacement field, but the interfacial fracture properties. We therefore focus next on the recovering of the interfacial stress distribution and its efficiency. The recovered traction profile, for case study #1, is illustrated in Fig. 9(a). Once the traction profile known, the displacement field is reconstructed and hence the opening profile results. The associated traction–separation relation is given in the insert of Fig. 9(a). The identified traction distribution as well as the traction–separation relation adequately fit most important characteristics of the input. The length of the opening zone (ℓ_o), the critical traction (t_c) and the physical crack tip position (x_0) are well captured. In addition, the assumed Winkler description, used in the I-DIC solution for $x > x_0$, is fairly well confirmed. Note however, that the adopted I-DIC procedure cannot capture the discontinuity at the maximum traction used in the bi-linear model. Indeed, the traction profile included in the kinematic description

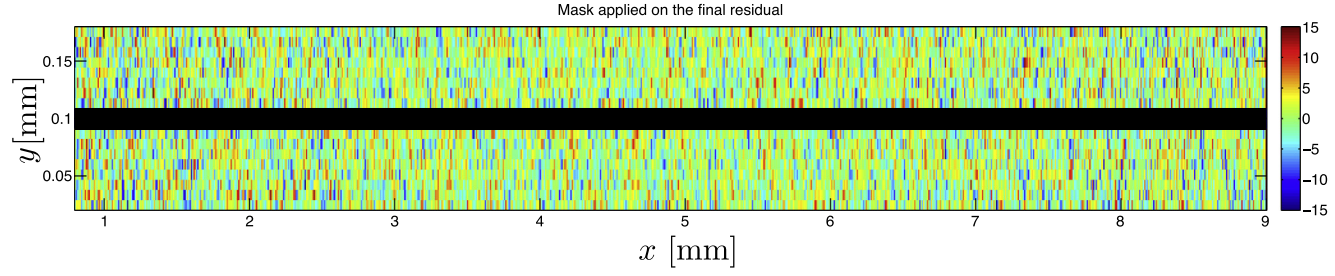

Fig. 7. Map of the residual at convergence for the I-DIC approach plotted at the reference undeformed specimen position (f). The data refers to study #1 and the black line at the center, *i.e.* the interface line, is a mask applied to the I-DIC to eliminate pixels close to the interface.

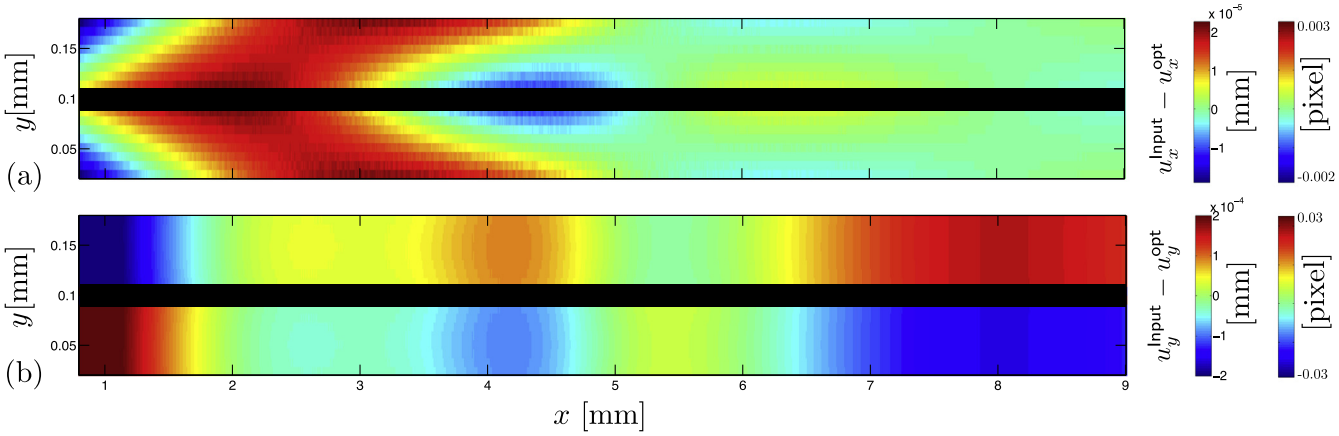

Fig. 8. X-error map (a) and y-error map (b) for case study #1 obtained from the reconstructed displacement fields from I-DIC and the input displacement fields from FEA, and they are plotted at the reference undeformed specimen position (f). The input FE fields are shown in Fig. 6. The black line at the center, *i.e.* the interface line, is a mask to eliminate pixels close to the interface.

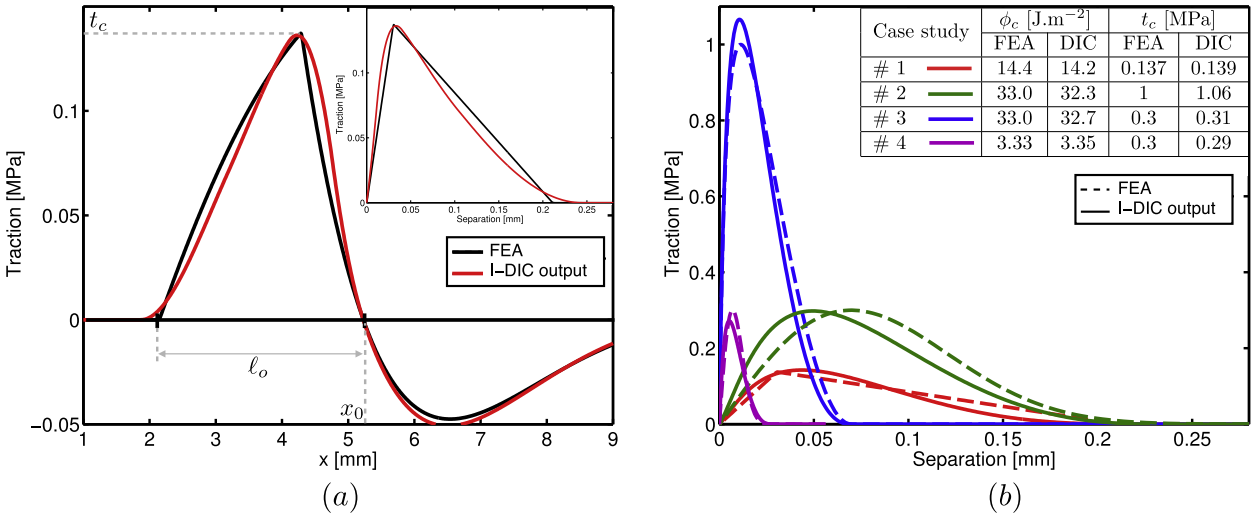

Case study	ϕ_c [J.m^{-2}]		t_c [MPa]	
	FEA	DIC	FEA	DIC
# 1	14.4	14.2	0.137	0.139
# 2	33.0	32.3	1	1.06
# 3	33.0	32.7	0.3	0.31
# 4	3.33	3.35	0.3	0.29

Fig. 9. (a) details on case study #1: traction profile (red line) obtained through the proposed I-DIC procedure from synthetic DCB fracture test data. The black line shows the output obtained from the finite element analysis. The insert shows the reconstructed traction–separation relation, which is obtained by combining the identified opening displacement and traction profile in the damaged (cohesive) region (FPZ); (b) comparison between input (dash lines) and output (continuous lines) traction–separation relations obtained for the different cases studies. White noise is applied to each case study with a standard deviation of 3% of the image dynamic range. (For interpretation of the references to color in this figure legend, the reader is referred to the web version of this article.)

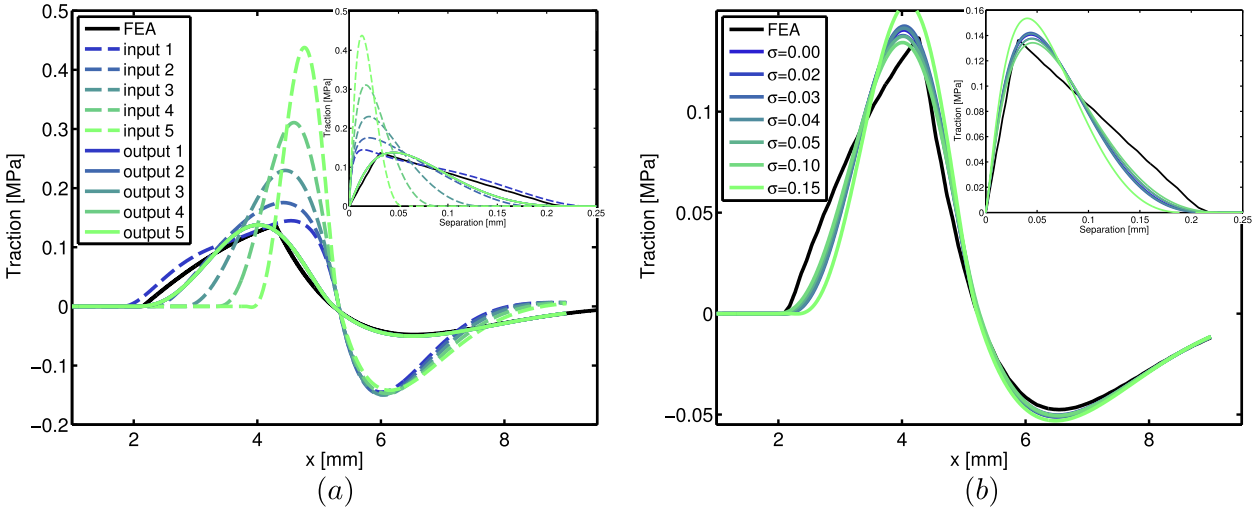

Fig. 10. (a) Identified traction profiles, obtained for different initial values of the degrees of freedom (input profiles). The reconstructed (output) profiles precisely overlap denoting the robustness of the method; (b) analysis of the effect of noisy data on the I-DIC procedure. The reconstructed traction–separation relations have been obtained for different standard deviations, σ of the white noise used in image (g). All results refer to case study #1.

has a polynomial form, which excludes such discontinuities. Using the same procedure, the cohesive properties for the other cases studies (#2–4) have been identified as well, see Fig. 9(b). The comparison of identified and input traction–separation relations reveals a reasonable match. In particular, the general shape of the traction–separation relation is well recovered, although a higher mismatch results for those cases characterized by a larger final opening displacement (Δ_c). Note that the work of separation (ϕ, *i.e.* the area under the curves) is always quite accurately estimated, as the deviation never exceeds 5%. In addition, the critical traction peak (t_c), which is usually difficult to recover, is adequately estimated.

From these results, it is obvious that the proposed method effectively recovers the interface fracture behavior, *i.e.* the traction profile and the corresponding traction–separation relation. The relatively small errors between the input traction–separation relation and the I-DIC reconstructions are due to an adequate parametrization of the interfacial traction profile within the FPZ. The relative errors of the cohesive parameters (t_c, Δ_c, ϕ_c) are larger than those of the displacement field, *cf.* Fig. 8, which is essentially due to the presence of image acquisition noise, *cf.* Fig. 7. This highlights the fact that an accurate description of the traction profile in the FPZ, based on a limited set of *dofs*, is essential to avoid amplification of the displacement error towards the final traction–separation relation.

5.2. Sensitivity to initial guess and robustness against noisy data

Next, the robustness of the method is assessed by examining (i) the sensitivity with respect the initial guess, and (ii) the robustness to noisy data – resembling actual experimental conditions. As specified earlier in Section 3.2, the complete traction profile is defined through the *dofs*, *i.e.* $\underline{\Lambda} = \{x_0, \ell_o, t_c\}$. To start the iterative method, an initial guess for $\underline{\Lambda}$ is required, see Fig. 1. A simple

dedicated I-DIC procedure, which is described in Appendix C, is employed for the initialization of x_0 and it yields the correct value of x_0 within ~ 0.1 [mm] accuracy. Subsequently, the initial choice of the remaining parameters is obtained by enforcing layer equilibrium:

$$F^+ = \int_{x_L}^{x_0} -t_{\text{linear}}(s)\mathrm{d}s = \frac{1}{2} t_c \times \ell_o, \tag{19}$$

where a linear traction profile t_{linear} is assumed. This gives a relation between the initial choice of ℓ_o and t_c. By using this constraint, a wide variety of initial sets for ℓ_o and t_c have been studied,whereas the initial guess of x_0 equals 5.32 [mm] (see Appendix C). The identification problem was solved to reveal the sensitivity to the initial guess. The results are reported in Fig. 10(a) showing that the obtained responses overlap, *i.e.* the I-DIC approach is insensitive to the choice of the initial guess.

Regarding the robustness to noisy data, we depart from the already depicted results, in which a white noise with a standard deviation of 3% was used to create the synthetic images.[7] The impact of increasing noise levels on the quality of the identified interface properties is next evaluated. To this aim, the traction profiles have been reconstructed for different noise levels. Case study #1 is considered for this purpose. Starting from a zero noise level we corrupted the images using a white noise with standard deviations σ ranging from 2% to 15%. Fig. 10(b) shows that noise levels up to $\sigma = 10\%$ do not affect the results, which remain comparable with the results from noiseless data. For noise levels $\sigma \geqslant 10\%$, the evaluation of the transition point x_0 remains accurate, but the traction peak and the size of FPZ are adversely affected. Therefore, it is concluded that the proposed procedure is noise robust as long as the images are recorded with a reasonable measurement noise level.

6. Conclusions

In the present work, a procedure has been proposed for the identification of the interfacial traction profile, and associated traction–separation relation, based on a DCB fracture test. The method roots in the recently developed Integrated Digital Image Correlation (I-DIC) approach. A mechanically admissible displacement field was obtained by incorporating a closed-form theoretical description that approximates the DCB test, which was coupled to the I-DIC algorithm. By minimizing the correlation residual with respect to the degrees of freedom, the unknown interfacial properties are identified in a one-step algorithm. The obtained results have shown that the most important features of the unknown traction–separation relation are adequately captured with the adopted set of *dofs*. The analysis of the spatial maps of the residual and the displacement errors revealed that the kinematic description is rich enough to capture all essential characteristics without yielding a high noise sensitivity. The procedure has shown to be robust with respect to the initial guess and noisy data, since it systematically recovered accurate estimation of the interfacial fracture properties.

Results shown are convincing. The main assumption on the interfacial properties concerns the parametrized traction distribution in the fracture process zone. To be as general as possible, a polynomial description was adopted. Nevertheless, this remains an open issue, and, for other cases better descriptions may be needed.

The proposed nonlinear I-DIC approach can be extended to different problems, including the identification of mixed-mode cohesive fracture properties of bonded samples, or bulk samples. The overall procedure will keep the same framework, while the kinematic description will be updated. Future work will address the application of the procedure to actual experimental data retrieved from in situ fracture testing of miniaturized beam-like samples.

Appendix A. Bernoulli beam problem description

As illustrated in Fig. 2(d), the DCB sample is modeled as two beams joined together through an interfacial region. The beams have Young's moduli E^+ and E^-, cross-sections S^+ and S^-, and second moments of area I^+ and I^-, respectively. The prescribed displacements $\left(v_p^+, v_p^-\right)$ are consequently applied to the beam neutral fibers, and the corresponding kinematic functions[8] are (i) the beam deflections $(v^+(x), v^-(x))$ and (ii) the cross-sectional rotations $(\theta^+(x), \theta^-(x))$. The latter are linked to the displacements through the well known kinematic relations $\theta^+(x) = \frac{\mathrm{d}v^+}{\mathrm{d}x}(x)$ and $\theta^-(x) = \frac{\mathrm{d}v^-}{\mathrm{d}x}(x)$. In order to incorporate the interfacial interaction, a normal traction distribution $t(x)(t^+(x) = -t(x), t^-(x) = t(x))$ is embedded in the model, Section 3.2. We denote $(M^+(x), M^-(x))$ and $(T^+(x), T^-(x))$ the beam bending moments and shear forces, respectively. Using the Bernoulli beam hypothesis, the governing equilibrium equations are:

$$\frac{\mathrm{d}M^\square}{\mathrm{d}x}(x) + T^\square(x) = 0 \quad \text{and} \quad \frac{\mathrm{d}T^\square}{\mathrm{d}x}(x) + t^\square(x) = 0, \tag{A.1}$$

In here, the box symbol "$\square$" denotes either the upper "+" or the lower layer, "−" respectively. The problem is subjected to the following boundary conditions:

$$v^\square(x_L) = v_p^\square \quad \text{and} \quad v^+(\infty) = v^-(\infty) \tag{A.2}$$

and:

$$M^\square(x_L) = 0 \quad \text{and} \quad M^\square(\infty) = 0. \tag{A.3}$$

In addition, the displacements and applied bending moments are related through the following constitutive relationship:

$$E^\square I^\square \frac{\mathrm{d}\theta^\square}{\mathrm{d}x}(x) = M^\square(x). \tag{A.4}$$

Using the previous equations and a given the traction profile $t(x)$, the problem can be solved and all kinematics quantities can be computed. In addition, since the opening displacement is applied at $x = x_L$, it is convenient to introduce the corresponding reaction force $T_F^\square = T^\square(x_L)$. The solution of the problem results in the load $T_F^\square$ resulting from the imposed displacements $v_p^\square$ at the left end of both beams.

Appendix B. Enforcement of stiffness continuity

The proposed theoretical description of the interfacial interactions requires stiffness continuity to be enforced at $x = x_0$. To this aim an additional term is added to the traction profile. First of all, we define the interfacial stiffness k of the DCB as follows:

$$k(x) \equiv \frac{\partial t}{\partial \Delta}(x) = \frac{1}{2}\frac{\partial t}{\partial v}(x) = \frac{1}{2}\frac{\partial t}{\partial x}(x)\left[\frac{\partial v}{\partial x}(x)\right]^{-1} = \frac{1}{2\theta(x)}\frac{\partial t}{\partial x}(x). \tag{B.1}$$

Noting that the cross-sectional rotation $\theta(x)$ is a continuous function by definition. Enforcing a continuous stiffness is therefore equivalent to requiring a continuous traction slope at x_0. The actual traction slope jump at $x = x_0$ is given by:

[7] Note that in common digital cameras the usual order of magnitude of the standard deviation of white noise approximately equals 1%, *i.e.* a conservative assumption has been made in this paper.

[8] Notice that since there is no applied loading in the axial direction, the axial forces do not enter the problem and consequently the axial displacements are equal to zero.

Table C.1
Results of the I-DIC procedure developed for the initialisation of x_0; all the dimensions are in [mm].

Case study	x_0 Dedicated I-DIC			FEA x_0
	Initial guess		Output	
1	1	→	5.32	5.24
2	1	→	4.21	4.24
3	1	→	4.33	4.26
4	1	→	3.35	3.30

$$\left[\!\left[\frac{\partial t}{\partial x}\right]\!\right]_{x=x_0} = \lambda t_w^0 - \frac{t_c \ell_o^2}{(x_c - x_0)(x_c - (x_0 - \ell_o))^2}. \tag{B.2}$$

Therefore, the continuity is restored by an additional term that is only active in the (FPZ) denoted by $t_k(x)$, which does not affect the global equilibrium (*i.e.* self-balanced). The resulting conditions to be enforced read:

$$\frac{\partial t_k}{\partial x}(x_0) = \left[\!\left[\frac{\partial t}{\partial x}\right]\!\right]_{x=x_0}, \tag{B.3}$$

$$\int_{x_0-\ell_o}^{\ell_o} \{t_k(x)\}\mathrm{d}x = 0, \tag{B.4}$$

$$\int_{x_0-\ell_o}^{\ell_o} \{(x_0 - x)t_k(x)\}\mathrm{d}x = 0. \tag{B.5}$$

A piece wise second order polynomial function $\mathbb{P}(x)$ has been adopted for this stiffness correction term t_k. To ensure its consistency with the traction profile definition, the following constraints are added:

$$\mathbb{P}(x_0) = 0, \quad \mathbb{P}(x_0 - \ell_o) = 0 \quad \text{and} \quad \mathbb{P}'(x_0 - \ell_o) = 0. \tag{B.6}$$

Then, one has

$$t_k(x) = \mathbb{P}(x)\Pi\left[\frac{1}{\ell_o}(x - (x_0 - \ell_o/2))\right], \tag{B.7}$$

where $\mathbb{P}$ is simply obtained from Eq. (B.6), but also from Eqs. (B.3)–(B.5).

Appendix C. Selection of an initial guess for x_0

A dedicated I-DIC procedure has been set-up to select a suitable initial guess for x_0. To this aim, simplified beam kinematics has been used, whereby both layers are modeled as two clamped Bernoulli beams and the interfacial interactions are not taken into account. The two beams are clamped at the position $x = x_0$ and subjected to a prescribed displacement. The I-DIC procedure is now used to solve a problem where the single *dof* employed in the kinematic description is given by x_0. The obtained solution is then used to initialize the main I-DIC algorithm to recover the traction profile at the interface. The results for the different cases studies presented in Section 5 are summarized in Table C.1. For each case study, this dedicated I-DIC was initialized with an arbitrary value of 1 [mm]. The comparison with the reference FEA shows that the resulting guess for x_0 is accurate within ~0.1 [mm].

References

Alfano, M., Lubineau, G., Furgiuele, F., Paulino, G.H., 2011. On the enhancement of bond toughness for Al/epoxy T-peel joints with laser treated substrates. Int. J. Fract. 171, 139–150.

Alfano, M., Lubineau, G., Furgiuele, F., Paulino, G.H., 2012. Study on the role of laser surface irradiation on damage and decohesion of Al/epoxy joints. Int. J. Adhes. Adhes. 39, 33–41.

Almuhammadi, K., Alfano, M., Yang, Y., Lubineau, G., 2014. Analysis of interlaminar fracture toughness and damage mechanisms in composite laminates reinforced with sprayed multi-walled carbon nanotubes. Mater. Des. 53, 921–927.

Andersson, T., Stigh, U., 2004. The stress-elongation relation for an adhesive layer loaded in peel using equilibrium of energetic forces. Int. J. Solids Struct. 41, 413–434.

ASTM, 2007. ASTM D5528-01(2007)e3: Standard Test Method for Mode I Interlaminar Fracture Toughness of Unidirectional Fiber-Reinforced Polymer Matrix Composites. ASTM International.

Avril, S., Bonnet, M., Bretelle, A.S., Grédiac, M., Hild, F., Ienny, P., Latourte, F., Lemosse, D., Pagano, S., Pagnacco, E., Pierron, F., 2008. Overview of identification methods of mechanical parameters based on full-field measurements. Exp. Mech. 48, 381–402.

Bao, G., Suo, Z., 1992. Remarks on crack-bridging concepts. Appl. Mech. Rev. 45, 355–366.

Barenblatt, G.I., 1962. The mathematical theory of equilibrium cracks in brittle fracture. Adv. Appl. Mech. 7, 55–129.

Besnard, G., Hild, F., Roux, S., 2006. Finite-element displacement fields analysis from digital images: application to Portevin–Le Châtelier bands. Exp. Mech. 46, 789–803.

Chandra, N., Li, H., Shet, C., Ghonem, H., 2002. Some issues in the application of cohesive zone models for metal–ceramic interfaces. Int. J. Solids Struct. 39, 2827–2855.

Dainty, J.C., 1977. The statistics of speckle patterns. Prog. Opt. 14, 1–46.

Dugdale, D.S., 1960. Yielding of steel sheets containing slits. J. Mech. Phys. Solids 8, 100–104.

Elices, M., Guinea, G.V., Gómez, J., Planas, J., 2002. The cohesive zone model: advantages, limitations and challenges. Eng. Fract. Mech. 69, 137–163.

Evans, A.G., Hutchinson, J.W., 1995. The thermomechanical integrity of thin films and multilayers. Acta Metall. Mater. 43, 2507–2530.

Fedele, R., Raka, B., Hild, F., Roux, S., 2009. Identification of adhesive properties in glare assemblies using digital image correlation. J. Mech. Phys. Solids 57, 1003–1016.

Gain, A.L., Carroll, J., Paulino, G.H., Lambros, J., 2011. A hybrid experimental/numerical technique to extract cohesive fracture properties for mode-I fracture of quasi-brittle materials. Int. J. Fract. 169, 113–131.

Gowrishankar, S., Mei, H., Liechti, K.M., Huang, R., 2012. A comparison of direct and iterative methods for determining traction–separation relations. Int. J. Fract. 177, 109–128.

Hild, F., Roux, S., 2006. Digital image correlation: from displacement measurement to identification of elastic properties – a review. Strain 42, 69–80.

Hild, F., Roux, S., 2012. Comparison of local and global approaches to digital image correlation. Exp. Mech. 52, 1503–1519.

Hild, F., Roux, S., Gras, R., Guerrero, N., Marante, M.E., Flórez-López, J., 2009. Displacement measurement technique for beam kinematics. Opt. Lasers Eng. 47, 495–503.

Hillerborg, A., Modéer, M., Petersson, P.E., 1976. Analysis of crack formation and crack growth in concrete by means of fracture mechanics and finite elements. Cem. Concr. Res. 6, 773–781.

Horn, B.K.P., Schunck, B.G., 1981. Determining optical flow. Artif. Intell. 17, 185–203.

Hutchinson, J.W., Evans, A.G., 2000. Mechanics of materials: top–down approaches. Acta Mater. 48, 125–135.

Hutchinson, J.W., Suo, Z., 1992. Mixed mode cracking in layered materials. Adv. Appl. Mech. 29, 63–191.

Ivankovic, A., Pandya, K.C., Williams, J.G., 2004. Crack growth predictions in polyethylene using measured traction–separation curves. Eng. Fract. Mech. 71, 657–668.

Jumel, J., Budzik, M.K., Shanahan, M.E.R., 2011. Process zone in the single cantilever beam under transverse loading. Part I: Theoretical analysis. Theor. Appl. Fract. Mech. 56, 7–12.

Kafkalidis, M.S., Thouless, M.D., 2002. The effects of geometry and material properties on the fracture of single lap-shear joints. Int. J. Solids Struct. 39, 4367–4383.

Kolluri, M., Thissen, M.H.L., Hoefnagels, J.P.M., van Dommelen, J.A.W., Geers, M.G.D., 2009. In-situ characterization of interface delamination by a new miniature mixed mode bending setup. Int. J. Fract. 158, 183–195.

Kolluri, M., Hoefnagels, J.P.M., van Dommelen, J.A.W., Geers, M.G.D., 2011. An improved miniature mixed-mode delamination setup for in situ microscopic interface failure analyses. J. Phys. D: Appl. Phys. 44, 034005.

Kolluri, M., Hoefnagels, J.P.M., Samimi, M., van Dommelen, H., van der Sluis, O., Geers, M.G.D., 2012. An in situ experimental-numerical approach for characterization and prediction of interface delamination: application to CuLF–MCE systems. Adv. Eng. Mater. 14, 1034–1041.

Leplay, P., Réthoré, J., Meille, S., Baietto, M.C., 2010. Damage law identification of a quasi brittle ceramic from a bending test using digital image correlation. J. Eur. Ceram. Soc. 30, 2715–2725.

Li, S., Thouless, M.D., Waas, A.M., Schroeder, J.A., Zavattieri, P.D., 2005. Use of a cohesive-zone model to analyze the fracture of a fiber-reinforced polymer–matrix composite. Compos. Sci. Technol. 65, 537–549.

Mathieu, F., Hild, F., Roux, S., 2012. Identification of a crack propagation law by digital image correlation. Int. J. Fatigue 36, 146–154.

Mello, A.W., Liechti, K.M., 2004. The effect of self-assembled monolayers on interfacial fracture. J. Appl. Mech. 73, 860–870.

Mitiche, A., Bouthemy, P., 1996. Computation and analysis of image motion: a synopsis of current problems and methods. Int. J. Comput. Vision 19, 29–55.

Mohammed, I., Liechti, K.M., 2000. Cohesive zone modeling of crack nucleation at bimaterial corners. J. Mech. Phys. Solids 48, 735–764.

Needleman, A., 1987. A continuum model for void nucleation by inclusion debonding. J. Appl. Mech. 54, 525.
Neggers, J., Hoefnagels, J.P.M., Hild, F., Roux, S., Geers, M.G.D., 2014. Direct stress–strain measurements from bulged membranes using topography image correlation. Exp. Mech. 54, 717–727.
Park, K., Paulino, G.H., 2012. Cohesive zone models: a critical review of traction–separation relationships across fracture surfaces. Appl. Mech. Rev. 64, 060802.
Park, K., Paulino, G.H., Roesler, J.R., 2009. A unified potential-based cohesive model of mixed-mode fracture. J. Mech. Phys. Solids 57, 891–908.
Réthoré, J., Hild, F., Roux, S., 2008. Extended digital image correlation with crack shape optimization. Int. J. Numer. Methods Eng. 73, 248–272.
Réthoré, J., Roux, S., Hild, F., 2009. An extended and integrated digital image correlation technique applied to the analysis of fractured samples. Eur. J. Comput. Mech. 18, 285–306.
Réthoré, J., Roux, S., Hild, F., 2011. Optimal and noise-robust extraction of fracture mechanics parameters from kinematic measurements. Eng. Fract. Mech. 78, 1827–1845.
Roux, S., Hild, F., 2006. Stress intensity factor measurements from digital image correlation: post-processing and integrated approaches. Int. J. Fract. 140, 141–157.
Roux, S., Hild, F., Viot, P., Bernard, D., 2008. Three-dimensional image correlation from X-ray computed tomography of solid foam. Compos. Part A: Appl. Sci. Manuf. 39, 1253–1265.
Samimi, M., van Dommelen, J.A.W., Geers, M.G.D., 2009. An enriched cohesive zone model for delamination in brittle interfaces. Int. J. Numer. Methods Eng. 80, 609–630.
Schreier, H., Orteu, J.J., Sutton, M.A., 2009. Image Correlation for Shape, Motion and Deformation Measurements: Basic Concepts, Theory and Applications. Springer.
Shen, B., Paulino, G.H., 2011. Direct extraction of cohesive fracture properties from digital image correlation: a hybrid inverse technique. Exp. Mech. 51, 143–163.
Sørensen, B.F., 2002. Cohesive law and notch sensitivity of adhesive joints. Acta Mater. 50, 1053–1061.
Sørensen, B.F., Jacobsen, T.K., 2003. Determination of cohesive laws by the *J* integral approach. Eng. Fract. Mech. 70, 1841–1858.
Srikanth, N., Chan, L., Vath III, C.J., 2006. Adhesion improvement of EMC leadframe interface using brown oxide promoters. Thin Solid Films 504, 397–400.
Swadener, J.G., Liechti, K.M., 1998. Asymmetric shielding mechanisms in the mixed-mode fracture of a glass/epoxy interface. J. Appl. Mech. 65, 25–29.
Tan, H., Liu, C., Huang, Y., Geubelle, P.H., 2005. The cohesive law for the particle/matrix interfaces in high explosives. J. Mech. Phys. Solids 53, 1892–1917.
Valoroso, N., Fedele, R., 2010. Characterization of a cohesive-zone model describing damage and de-cohesion at bonded interfaces. Sensitivity analysis and mode-I parameter identification. Int. J. Solids Struct. 47, 1666–1677.
Van den Bosch, M.J., Schreurs, P.J.G., Geers, M.G.D., 2006. An improved description of the exponential Xu and Needleman cohesive zone law for mixed-mode decohesion. Eng. Fract. Mech. 73, 1220–1234.
Wang, J.T., 2013. Investigating some technical issues on cohesive zone modeling of fracture. J. Eng. Mater. Technol. 135, 011003.
Zhu, Y., Liechti, K.M., Ravi-Chandar, K., 2009. Direct extraction of rate-dependent traction–separation laws for polyurea/steel interfaces. Int. J. Solids Struct. 46, 31–51.